A Whole-Body Imaging Technique for Tumor-Specific Diagnostics and Screening of B7-H3-Targeted Therapies

Lei Xia[1]†*, Yan Wu[2]†, Yanan Ren[3]†, Zhen Wang[4]†, Nina Zhou[1], Wenyuan Zhou[1], Lixin Zhou[2], Ling Jia[2], Chengxue He[1], Xiangxi Meng[1], Hua Zhu[1], Zhi Yang[1]*

[1]Key Laboratory of Carcinogenesis and Translational Research (Ministry of Education/Beijing), NMPA Key Laboratory for Research and Evaluation of Radiopharmaceuticals (National Medical Products Administration), Department of Nuclear Medicine, Peking University Cancer Hospital & Institute, Beijing, China.

[2]Key laboratory of Carcinogenesis and Translational Research (Ministry of Education/Beijing), Department of Pathology, Peking University Cancer Hospital & Institute, Beijing, China.

[3]Department of Nuclear Medicine, Affiliated Hospital of Zunyi Medical University, Zunyi, Guizhou, China.

[4]Key Laboratory of Carcinogenesis and Translational Research (Ministry of Education, Beijing), Department of Hepato-Pancreato-Biliary Surgery, Sarcoma Center, Peking University Cancer Hospital and Institute, Beijing, China.

†These authors contributed equally to this work

*Corresponding authors

Lei Xia, Peking University Cancer Hospital & Institute, 52 Fucheng Rd., Beijing

100142, China. Tel: +86-010-88197852, Email: xialei9012288@126.com

Zhi Yang, Peking University Cancer Hospital & Institute, 52 Fucheng Rd., Beijing

100142, China. Tel: +86-010-88196196, Email: pekyz@163.com

Conflict-of-interest:

The authors have declared that no conflict of interest exists.

ABSTRACT

Background

B7-H3 or CD276 is notably overexpressed in various malignant tumor cells in humans, with extremely high expression rates. The development of a radiotracer that targets B7-H3 may provide a universal tumor-specific imaging agent and allow the noninvasive assessment of the whole-body distribution of B7-H3-expressing lesions.

Methods

We enhanced and optimized the structure of an affibody (ABY) that targets B7-H3 to create the radiolabeled radiotracer [**^{68}Ga]Ga-B7H3-BCH**, and then, we conducted both foundational experiments and clinical translational studies.

Results

[**^{68}Ga]Ga-B7H3-BCH** exhibited high affinity (Kd=4.5 nM), and it was taken up in large amounts by B7-H3-transfected cells (A549^{CD276} and H1975^{CD276} cells); these phenomena were inhibited by unlabeled precursors. Moreover, PET imaging of multiple xenograft models revealed extensive [**^{68}Ga]Ga-B7H3-BCH** uptake by tumors. In a clinical study including 20 patients with malignant tumors, the [**^{68}Ga]Ga-B7H3-BCH** signal aggregated in both primary and metastatic lesions, surpassing ^{18}F-FDG in overall diagnostic efficacy for tumors (85.0% vs 81.7%), including differentiated hepatocellular and metastatic gastric cancers. A strong correlation between B7-H3 expression and [**^{68}Ga]Ga-B7H3-BCH** uptake in tumors was observed, and B7-H3 expression was detected with 84.38% sensitivity and 100% specificity when an SUVmax of 3.85 was set as the cutoff value. Additionally, B7-H3-specific PET imaging

64 is expected to predict B7H3 expression levels in tumor cells, intratumoral stroma and

65 peritumoral tissues.

Conclusion

67 In summary, **[⁶⁸Ga]Ga-B7H3-BCH** has potential for the noninvasive identification of

68 B7H3 expression in systemic lesions in patients with malignant tumors. This agent has

69 prospects for improving pretreatment evaluation, predicting therapeutic responses, and

70 monitoring resistance to therapy in patients with malignancies.

Trial registration

72 ClinicalTrials.gov NCT06454955.

INTRODUCTION

B7-H3, which is sometimes called CD276, is a transmembrane glycoprotein B7 family member and a T cell regulator. B7-H3 is notably and selectively overexpressed in different subtypes of human malignant tumor cells compared with normal tissues and benign lesions (1,2). B7-H3 is a cell surface receptor protein that is closely associated with tumor resistance, metastasis, and immune modulation (3-5). Additionally, B7-H3 is overexpressed on endothelial cells of the tumor vasculature, while it is expressed at low levels or not expressed in normal tissues (6-8). These characteristics make B7-H3 an ideal candidate target for therapeutic agents that aim to ablate tumor cells and the tumor vasculature with high specificity. According to recent studies, B7-H3-targeted antibody–drug conjugates (ADCs) demonstrate considerable potential for the treatment of various types of tumors. In fact, multiple pharmaceutical companies have started developing strategies that target this antigen (9-11). Academically, the presence and abundance of a target are still considered critical factors that determine the therapeutic efficacy of targeted treatment approaches (12). However, the methods for detecting B7-H3 expression in tumors are still limited to invasive histopathological examinations. Owing to the heterogeneity of tumors, determining the expression of therapeutic targets around and within metastatic lesions is challenging; this complicates pretreatment assessments of patient responses to treatment (13). With the development of targeted radiotracers, nuclear medicine techniques allow the high-specificity diagnosis of systemic B7-H3 expression. Such methods qualitatively and quantitatively reveal receptor expression in primary and systemic metastatic lesions, thus facilitating precise

5

diagnosis and predicting the efficacy and prognosis of targeted therapies (14-16).

Currently, radionuclide therapeutic agents that target B7H3 have reached the forefront of clinical research. Kramer et al. (17) designed a targeted radionuclide therapeutic radiotracer by labeling a monoclonal antibody with ^{131}I. The findings revealed that the radionuclide probe was safe, and survival was increased compared to the historical data among treated neuroblastoma patients. Additionally, Burvenich et al. (18) constructed a targeted PET imaging probe using an anti-B7H3 antibody that was labeled with a radionuclide with a long half-life; this probe achieved favorable imaging results in animal models. However, the widespread clinical application of antibody-based radiotracers is limited by several challenges, including prohibitive costs and the potential of these radiotracers to elicit immune responses, especially under conditions of repeated administration (19). Previous research has shown that smaller protein fragments can facilitate efficient, locus-specific binding, and such fragments are increasingly replacing antibodies in tumor diagnostic research **(20,21)**. Affibodies (ABYs), which are promising binding ligands for designing molecular imaging tools, are small, 58-amino acid proteins with a molecular weight of approximately 7 kDa (22,23). Compared with antibodies, ABYs demonstrate faster nonspecific clearance, greater biocompatibility, and better stability both in vivo and in vitro, making them better suited for widespread production and site-specific binding (24). A recent report highlighted the use of a highly specific ABY named AC12 to target B7-H3, and AC12 has robust affinity, favorable biocompatibility, and optimal pharmacokinetic properties (25). A series of foundational studies were previously reported (26,27). Oroujeni et

130   al.(28) used this affinity ligand to construct a ^{99m}Tc-labeled imaging probe, which

131   achieved favorable SPECT imaging results in a mouse tumor model. It is believed that

132   such an ABY would be well suited for adaptation for use in PET molecular imaging.

133   In this study, we aimed to develop a radiotracer, namely, **[^{68}Ga]Ga-B7H3-BCH**,

134   that specifically targets B7-H3 for use in PET imaging of various tumor types and to

135   advance this radiotracer into clinical translation studies. This radiotracer was designed

136   to allow the specific, noninvasive evaluation of B7-H3 expression in all bodily lesions,

137   and it is expected to overcome some limitations of nonspecific false-negative results

138   that are inherent to ^{18}F-FDG imaging. Furthermore, we explored the potential impact

139   of tumor B7H3 distribution on the uptake of this targeted radiotracer. This advanced

140   capability is expected to enable the exhaustive exploration of the biological interactions

141   among the radiotracer, the B7H3 protein, and cellular components.

142

143

144

145

146

147

148

149

150

151

RESULTS

B7H3-targeting ABY improvement, synthesis and quality control

Our initial efforts focused on replicating the synthesis of the AC12 structure and conjugating it with the bifunctional chelator DOTA to create a molecular probe (Figure 1A); additionally, the resulting probe was subjected rigorous quality control (Supplementary Figure S1). However, the fundamental results of the evaluation of the ^{68}Ga-DOTA-AC12 probe failed to meet the criteria necessary for clinical application. Consequently, we sought to optimize the molecule by generating a ABY structure, namely, Resca-B7H3-BCH (Figure 1B).

In our redesign, the N-terminus of the ABY structure was modified using 1-amino-3,6,9,12-tetraoxapentadecan-15-oic acid (PEG4). Additionally, we introduced two units of 6-aminohexanoic acid (Acp) at the C-terminus. Then, we used the bifunctional coupling agent H3RESCA-TFP instead of DOTA to modify the probe. The molecular weight and mass dose of ^{68}Ga-B7H3-BCH were 7269 g/mol and 7400 GBq/kg, respectively, and it exhibited a high specific activity of up to 53.3 GBq/μmol. As a result, pharmacokinetic analysis revealed that the elimination half-life of [^{68}**Ga]Ga-B7H3-BCH** increased from 10.31 minutes to 28.34 minutes (Figure 1C vs. Figure 1D). By extending the plasma half-life of the probe's distribution phase, reducing its rapid clearance and increasing its uptake at the target site. Studies of probe distribution in normal mice demonstrated that compared with ^{68}Ga-DOTA-AC12, [^{68}**Ga]Ga-B7H3-BCH** exhibited a marked reduction in renal uptake, with renal uptake peaks decreasing by approximately fivefold (721.7±22.0 %ID/g vs. 160.8±12.7 %ID/g) and exhibiting a

8

174 rapid decrease over time; these results represented a substantial improvement over the

175 unmodified structure (Figure 1, E and F, Supplementary Table S1 and S2). Moreover,

176 the process of labeling the probe with H3RESCA-TFP was considerably milder,

177 requiring only room temperature to achieve extremely high labeling efficiency and

178 radiochemical purity (Supplementary Table S3); this process can prevent potential

179 damage to the ABY structure. The improved synthesis method and complete structural

180 formula of Resca-B7H3-BCH are shown in Supplementary Figure S2 and S3, and the

181 comprehensive quality control results are shown in Supplementary Figure S4.

182

183 **Affinity testing and enhanced PET imaging of the [^{68}Ga]Ga-B7H3-BCH**

184 **radiotracer**

185 [^{68}Ga]Ga-B7H3-BCH exhibited good stability in vitro after a series of modifications

186 (Supplementary Figure S6). Binding affinity assays revealed that this radiotracer

187 exhibited a slightly greater binding affinity (Kd: 4.5 nM) than did ^{68}Ga-DOTA-AC12

188 (Kd: 8.3 nM) (Figure 1, G and H). Further analysis via surface plasmon resonance (SPR)

189 revealed that Resca-B7H3-BCH had an equilibrium dissociation constant of 6.91 nM

190 (Supplementary Figure S5). Moreover, we noted a substantial reduction in nonspecific

191 [^{68}Ga]Ga-B7H3-BCH uptake by most organs (Figure 1, E and F). Through radiation

192 dose estimation, we determined that [^{68}Ga]Ga-B7H3-BCH had an effective dose of

193 only 1.19E-02 mGy/MBq, which was approximately one-third that of the effective dose

194 of ^{68}Ga-DOTA-AC12 (3.31E-02 mGy/MBq) (Supplementary Table S4 and S5). In

195 particular, the radiation dose for the kidney as a single organ decreased from 1.87

mGy/MBq to 0.59 mGy/MBq, which was a safe range. This decrease markedly

improved the safety and applicability of the radiotracer in various clinical settings.

Head-to-head microPET/CT imaging also demonstrated the superiority of [^{68}**Ga]Ga-**

B7H3-BCH in a human lung cancer xenograft model derived from B7H3-transfected

H1975 cells; these cells were confirmed to exhibit high B7H3 expression by IHC

(Figure 1J). During the 2-hour dynamic imaging session, [^{68}**Ga]Ga-B7H3-BCH**

showed marked greater uptake at the tumor site than ^{68}Ga-DOTA-AC12 did (Figure 1I).

Additionally, statistical analysis revealed that the tumor-to-nontumor tissue (T/NT)

standardized uptake value maximum (SUVmax) ratio was greater for [^{68}**Ga]Ga-B7H3-**

BCH (7.43 vs. 4.12 at 2 hours), indicating a higher target-to-background ratio (TBR).

Furthermore, the TBR peaked at approximately 1 hour and gradually decreased

thereafter, providing a reference for determining the optimal imaging time points for

subsequent clinical translational imaging studies (Figure 1K).

Functional evaluation of the [^{68}Ga]Ga-B7H3-BCH radiotracer

[^{68}**Ga]Ga-B7H3-BCH** had highly stable affinity for the B7H3 protein. Its biomolecular

targeting efficacy was verified through in vitro cellular assays (Figure 2A). B7H3-

transfected A549^{CD276} and H1975^{CD276} cells were engineered and subsequently

characterized by Western blotting (Figure 2B). The accumulation of [^{68}**Ga]Ga-B7H3-**

BCH in transfected cells substantially exceeded that in non-transfected cells, and this

accumulation could be competitively inhibited by cold precursors. Additionally, the

maximum uptake typically occurred at 30 minutes, followed by a decrease at 60

10

minutes. Furthermore, cellular internalization experiments demonstrated that [**^{68}Ga]Ga-B7H3-BCH** was internalized by cells at a high rate, but it was rapidly effluxed from the cells, achieving dynamic equilibrium by 60 minutes; these results suggested optimal timing for in vivo imaging evaluations (Figure 2C).

PET/CT imaging was performed with [**^{68}Ga]Ga-B7H3-BCH** in various xenograft models, including human bladder cancer, colon cancer, glioma, lung cancer and stomach cancer xenograft models (Figure 2D). Micro-PET/CT images were obtained at 1 and 2 hours postinjection. Additionally, two patient-derived xenograft (PDX) models, including renal carcinoma and gastric cancer PDX models, were subjected to PET/CT imaging (Supplementary Figure S7 and S8). The images revealed heterogeneous uptake of [**^{68}Ga]Ga-B7H3-BCH** at tumor sites in all the xenograft models, which was consistent with the immunohistochemical findings from the tumor sections (Figure 2, E and F). PET/CT imaging and statistical analysis revealed a reduction in [**^{68}Ga]Ga-B7H3-BCH** uptake by tumor at 2 hours compared with that at 1 hour, the magnitude of which varied among the different models. Specifically, the H3122 and BGC823 models exhibited a more decrease than the SW780, LS174T, and U87 models did (Figure 2E). Moreover, a detailed comparison of the immunohistochemical staining intensities revealed diverse B7H3 expression levels across the five models. Notably, the SW780, LS174T, and U87 models exhibited regions with strong B7H3 positivity (B7H3 *3+*), whereas the H3122 and BGC823 models lacked strong B7H3 positivity but still maintained an overall score (Figure 2G); this potentially accounts for the brief retention times of the [**^{68}Ga]Ga-B7H3-BCH** probe within these tumor sites.

Preclinical preparation and safety evaluation of the [^{68}Ga]Ga-B7H3-BCH radiotracer

A key component of our preclinical studies involved the use of the A549^{CD276} xenograft mouse model to investigate both the biodistribution and the blocking ability of the [^{68}Ga]Ga-B7H3-BCH radiotracer. The data that were collected one hour postinjection revealed a marked increase in tracer uptake at the tumor sites compared with that in the blocked group (Figure 2H). Moreover, most organs in the blocked group exhibited reduced uptake, suggesting the potential for residual nonspecific uptake. Additionally, on the basis of the in vivo distribution of [^{68}Ga]Ga-B7H3-BCH in mice, the effective radiation dose in human was calculated to be 1.19E-2 mGy/MBq (Supplementary Table S5), which is below the FDA's imposed limit for research purposes (29). The safety of the [^{68}Ga]Ga-B7H3-BCH radiotracer was thoroughly evaluated by toxicological testing. Compared with control mice, normal mice that were administered an overdose of [^{68}Ga]Ga-B7H3-BCH (37 MBq/per mouse, n=5) presented no marked change in body weight, and tests revealed normal liver function and blood indicators as well as standard hematological parameters (Supplementary Figure S9). Histopathological examination by hematoxylin and eosin (HE) staining was conducted ten days postinjection, and the results revealed no pathological changes in major organs relative to those of the controls (Supplementary Figure S10).

Clinical translation study of the [^{68}Ga]Ga-B7H3-BCH radiotracer

262 This clinical study included 20 patients with various types of malignant tumors.

263 Detailed participant information is provided in Table 1 and Supplementary Table S7.

264 The PET scanning followed the protocols and dynamic reconstruction methods shown

265 in Figure 3 and Supplementary Figure S11. Each scanning session lasted approximately

266 5 minutes, which was approximately one-quarter of the duration of conventional

267 PET/CT scans; thus, patient comfort during the procedure was increased. Each patient

268 received 1.42 MBq/kg [^{68}Ga]Ga-B7H3-BCH, which was approximately one-third of

269 the dose that is typically used in traditional PET exams. The effective radiation dose of

270 ^{68}Ga-B7H3-BCH in humans is 7.02E-02 mGy/MBq (Table S6), which is slightly

271 greater than the effective radiation dose in a mouse model that simulates human

272 exposure (1.19E-2 mGy/MBq). Nevertheless, this dose was low, indicating a high

273 degree of radiation safety, and no adverse effects associated with the injection of the

274 radiotracer and PET/CT scanning were observed in any of the enrolled patients.

275 Comprehensive multi-timepoint, multi-slice dynamic images (including maximum-

276 intensity projection (MIP) and axial and coronal views) as well as a complete dynamic

277 reconstruction video of a patient who underwent imaging [^{68}Ga]Ga-B7H3-BCH can

278 be found in Supplementary Figure S12 and Video S1, respectively. The radiotracer's

279 temporal distribution curves within tissues were generated via total-body PET/CT

280 (Figure 4A). Notably, kidney uptake gradually increased during the first hour, whereas

281 other organs, such as the spleen, lungs, liver, and aorta, exhibited rapid initial uptake

282 followed by gradual decreases in uptake. Conversely, radiotracer uptake in the brain

283 remained consistently low, suggesting the need for further research on whether

284 **[^{68}Ga]Ga-B7H3-BCH** is hindered by the blood–brain barrier.

285 Static imaging of all the included patients was performed 50–60 minutes

286 postinjection; this timepoint was initially chosen on the basis of dynamic imaging in

287 mice, which indicated that the highest TBR at the tumor site was observed at 50–60

288 minutes postinjection (Figure 1I). Delayed imaging did not yield better results, as the

289 probe was rapidly cleared from the tumor site at 1 hour after injection (Supplementary

290 Figure S13). Regions of interest (ROIs) were delineated in 19 major organs, and a

291 statistical analysis of the SUVmax was conducted (Figure 4B). The kidneys continued

292 to exhibit high uptake, although immunohistochemistry confirmed that normal kidney

293 tissues did not show high levels of B7H3 expression (Figure 4C), indicating that the

294 radiotracer was primarily excreted through the urinary system, and renal retention was

295 observed. The liver, uterus, and prostate demonstrated comparatively higher uptake,

296 and some B7H3 expression within the interstitium of normal liver and prostate tissues

297 were observed by immunohistochemistry; the uptake of other organs generally

298 corresponded with the immunohistochemical results.

299 Dynamic imaging effectively reveals the temporal distribution for lesions,

300 facilitating the selection of the most suitable imaging timepoints. As shown in Figure

301 4D, the SUVmax of the three tumor groups peaked between 120 and 150 seconds after

302 the injection of **[^{68}Ga]Ga-B7H3-BCH**, followed by a rapid decrease. While Dynamic

303 scan 1 shows a gradually slowing reduction, the other two measurements were either

304 stable or slowly decreased. The time distribution curves of the tumor-to-aorta ratio

305 across the three patients showed a gradual increase within the first 50 minutes, followed

306 by stabilization (Figure 4E). Accordingly, conducting PET/CT imaging between 50 and

307 60 minutes postinjection is consistent with the optimal imaging time.

308

309 **Use of the [⁶⁸Ga]Ga-B7H3-BCH for the diagnosis of diverse tumor types**

310 B7H3 is widely expressed by malignant tumors. Thus, twenty patients with various

311 malignancies were evaluated via **[⁶⁸Ga]Ga-B7H3-BCH** and ¹⁸F-FDG PET/CT. The

312 patient cohort included four patients with lung cancer; three patients with melanoma;

313 two patients with colon cancer; two patients with lymphoma; two patients with liver

314 cancer; two patients with stomach cancer; two patients with esophageal cancer; one

315 patient with metastatic lymph nodes of unknown origin; one patient with rectal cancer;

316 and one patient with breast cancer (Supplementary Table S7). The MIP images shown

317 in Figure 5 highlight the uptake of **[⁶⁸Ga]Ga-B7H3-BCH** across the ten different tumor

318 types, revealing varied levels of radiotracer uptake with SUVmax values ranging from

319 3.7 to 10.7. These images highlight the strong efficacy of **[⁶⁸Ga]Ga-B7H3-BCH** for

320 the diagnosis of melanoma, breast cancer, lung cancer, gastric cancer and esophageal

321 cancer, which is principally attributed to the distinct demarcation of lesions against a

322 clear background and a superior signal-to-noise ratio. Furthermore, imaging in a

323 melanoma patient demonstrated that **[⁶⁸Ga]Ga-B7H3-BCH** could allow the detailed

324 visualization of both primary and multiple metastatic sites, achieving imaging results

325 comparable to those of ¹⁸F-FDG (Supplementary Figure S14). In parallel, PET imaging

326 in other patients demonstrated low uptake in some lesions, including in certain patients

327 with lung or colon cancer, indicating tumor heterogeneity in the PET imaging of

328 **[^{68}Ga]Ga-B7H3-BCH (**Supplementary Figure S15**). [^{68}Ga]Ga-B7H3-BCH** shows

329 potential as a specific imaging agent for multiple tumors, as it can be used to resolve

330 misdiagnoses due to the nonspecific uptake of ^{18}F-FDG.

331

332 **Head-to-head comparative of [^{68}Ga]Ga-B7H3-BCH and ^{18}F-FDG imaging**

333 In a study involving 20 patients, 60 tumor lesions were identified, including 21 primary

334 and 39 metastatic sites (verified through histopathology and various imaging

335 modalities). The **[^{68}Ga]Ga-B7H3-BCH** PET identified 51 lesions (85.0%; 18 primary

336 and 33 metastatic), whereas the ^{18}F-FDG PET detected 49 lesions (81.7%; 19 primary

337 and 30 metastatic lesions) (Supplementary Table S8). Additionally, 70.0% of these

338 lesions (42 out of 60) tested positive for both **[^{68}Ga]Ga-B7H3-BCH** and ^{18}F-FDG. A

339 further 9 lesions (15.0%) were positive for **[^{68}Ga]Ga-B7H3-BCH** but negative for ^{18}F-

340 FDG, which included 1 primaries and 9 metastases. Morphological imaging and follow-

341 up assessments confirmed that merely 3.3% of the lesions (2 out of 60) were negative

342 for both tracers, involving one metastatic melanoma lymph node and one colon cancer

343 lesion.

344 Comparisons were made between SUVmax and target-to-muscle ratios (TMR) from

345 **[^{68}Ga]Ga-B7H3-BCH** and ^{18}F-FDG PET/CT (Table 2). While the SUVmax values for

346 most tumor types were generally lower on the **[^{68}Ga]Ga-B7H3-BCH** PET/CT

347 compared to the ^{18}F-FDG PET/CT, an exception was noted in liver cancer and

348 metastasis of gastric cancer where the uptake was higher. Statistically significant

349 differences were only observed in patients with melanoma and lymphoma. Regarding

the TMR, excluding lymphoma, there were no significant differences between the imaging techniques across the various tumor types. Numerically, the TMR values for the [^{68}Ga]Ga-B7H3-BCH displayed a marked improvement compared with SUVmax, markedly reducing the discrepancy observed with the ^{18}F-FDG uptake across most tumor types.

Association between [^{68}Ga]Ga-B7H3-BCH uptake and B7H3 expression

We obtained 12 pretreatment pathological biopsy samples from primary tumor sites in 12 patients, including two patients with colon cancer, two patients with lung cancer, two patients with liver cancer, two patients with stomach cancer, one patient with esophageal cancer, one patient with breast cancer, one patient with melanoma, and one patient with a metastatic lymph node of unknown origin. Then, we performed immunohistochemical staining for the B7H3 protein on these samples. Static imaging with [^{68}Ga]Ga-B7H3-BCH demonstrated high uptake in lesion of a patient with well-differentiated hepatocellular carcinoma, and this high uptake was associated with strong positive immunohistochemical staining (B7H3 *3+*) that was observed in the lesion biopsy (Figure 6A). Furthermore, high uptake was observed in the lesion of a breast cancer patient, and immunohistochemical staining revealed a B7H3 expression level of B7H3 *2+* (Figure 6B); however, lower uptake was observed in the lesion of a lung cancer patient with weak B7H3 expression (B7H3 *1+*) (Figure 6C). We then performed statistical analysis comparing all the measurable lesions with the results of immunohistochemical staining of primary tumor cells; all the lesions that were

372 analyzed were confirmed to be metastases or primary sites by three experienced nuclear

373 medicine physicians with CT and ^{18}F-FDG PET/CT.

374   The uptake of [^{68}Ga]Ga-B7H3-BCH in tumors with B7H3 *3+* and B7H3 *2+*

375 expression was marked greater than that in B7H3 *1+* expression (SUVmax: 5.6±1.9 vs

376 4.7±1.0 vs 3.0±0.5), A positive correlation was identified significantly between

377 [^{68}Ga]Ga-B7H3-BCH uptake and B7H3 expression levels (Figure 6D-E, $P < 0.005$).

378 In addition, ^{18}F-FDG was taken up in large amounts by most lesions, but there was no

379 significant difference in uptake with ^{18}F-FDG as evaluation criteria (Supplementary

380 Figure S16, $P > 0.005$).

381   The receiver operating characteristic (ROC) curves were generated to determine the

382 specificity of [^{68}Ga]Ga-B7H3-BCH for B7H3-targeted screening. The area under the

383 curve (AUC) was 0.9707 for [^{68}Ga]Ga-B7H3-BCH at 50–60 minutes of static imaging

384 (95% CI, 92.49% to 100%) and only 0.5300 for ^{18}F-FDG at 50–60 minutes of static

385 imaging (95% CI, 32.15% to 73.85%, Figure 6F). These findings demonstrated that

386 [^{68}Ga]Ga-B7H3-BCH PET imaging has high specificity for the clinical detection of

387 the B7H3 receptor. When an SUVmax of 3.85 was set as the cutoff to discriminate

388 tumors with B7H3 *3+* or B7H3 *2+* expression via [^{68}Ga]Ga-B7H3-BCH PET/CT

389 imaging, the sensitivity and specificity were 84.38% (95% CI, 68.25% to 93.14%) and

390 100.0% (95% CI, 67.56% to 100%), respectively. Overall, [^{68}Ga]Ga-B7H3-BCH

391 PET/CT imaging demonstrated excellent sensitivity and specificity for detecting B7H3-

392 expressing lesions compared with ^{18}F-FDG.

393

Imaging advantages and influence of variable B7H3 expression

The methods that can be used to diagnose gastric cancer with peritoneal metastasis by imaging are limited. Despite the high sensitivity of ^{18}F-FDG for most peritoneal metastases, early peritoneal gastric cancer metastases, particularly those involving signet ring cell components, may still be missed. Figure 7, A-D shows a patient with peritoneal metastasis that was missed by ^{18}F-FDG, and the patient was subsequently subjected to **[^{68}Ga]Ga-B7H3-BCH** PET/CT imaging. Both imaging methods revealed marked uptake by the gastric lesion, indicating similar diagnostic effectiveness, but **[^{68}Ga]Ga-B7H3-BCH** imaging revealed multiple peritoneal metastatic sites with high uptake (SUVmax 6.8), in contrast to the low uptake that was observed by ^{18}F-FDG imaging (SUVmax <1.5). The lesion near the upper part of the colon, which was initially diagnosed as colonic inflammation by ^{18}F-FDG imaging, was considered to be peritoneal metastasis by a nuclear medicine physician who examined the **[^{68}Ga]Ga-B7H3-BCH** imaging results. This result changed the patient's staging and the chosen surgical approach; this outcome aligned with the primary intention of this study, namely, to develop molecular probes and explore their clinical translation to benefit the patients who were involved in the study.

Numerous studies have shown that B7H3 is not only expressed in tumor cells but also prominently expressed in tumor stromal cells and peritumoral tissues (1,30,31). We evaluated images of immunohistochemical staining of lesions from 12 patients to assess B7H3 expression in three distinct areas, namely, tumor cells, intratumoral stroma and peritumoral tissues. Owing to the limited number of samples, it was not possible to

19

determine whether the distribution of B7H3 expression was associated with specific

tumor types. However, by comparing differences in B7H3 distribution with [^{68}**Ga]Ga-**

B7H3-BCH uptake, we revealed that B7H3 *3+* and B7H3 *2+* expression in tumor cells

was a necessary condition for achieving SUVmax values above the pre-established

cutoff of 3.85 (Figure 7, E, F, H and I; Supplementary Figure S17, A-C and F). High

B7H3 expression in the tumor stroma alone did not result in [^{68}**Ga]Ga-B7H3-BCH**

uptake (Figure 7, G and J; Supplementary S17, D and E). Moreover, B7H3 expression

in the tissues surrounding the tumor did not markedly affect [^{68}**Ga]Ga-B7H3-BCH**

uptake. Additionally, high B7H3 expression within both tumor cells and surrounding

tissues was associated with increased SUVmax values (Figure 7, E and I). Further

studies with larger samples are needed to confirm these observations.

DISCUSSION

We have successfully developed an ABY radiotracer that specifically targets the B7H3 receptor protein, and we completed a series of studies ranging from basic research to clinical translation. [^{68}**Ga]Ga-B7H3-BCH** has high affinity, good stability in vitro and in vivo, satisfactory pharmacokinetic parameters, and very high safety. Total-body PET/CT full dynamic imaging revealed the temporal distribution of the radiotracer in critical human organs and the optimal timing for lesion visualization. PET/CT images showed the specific diagnostic capabilities of [^{68}**Ga]Ga-B7H3-BCH** for various malignancies, particularly its advantages in the diagnosis of well-differentiated hepatocellular carcinoma and gastric cancer peritoneal metastasis. This radiotracer exhibits high specificity and sensitivity in detecting B7H3 expression, making it suitable for noninvasive exploration of primary and metastatic lesions throughout the body.

Previous studies involving B7H3-targeted radiotracers have primarily used monoclonal antibodies as carriers (17,18). In contrast, ABY-based probes can rapidly accumulate at target sites and are quickly cleared from the body, facilitating the use of short-lived radionuclides for imaging purposes. A prior study utilized ^{99m}Tc-labeled AC12 to create single-photon imaging probes for use in foundational experiments (28). However, the limitations inherent to SPECT imaging technology prevented the achievement of optimal imaging outcomes. Employing positron-emitting radionuclides to label ABYs and leveraging the latest advances in high-precision PET/CT imaging technology can achieve superior imaging results, increasing the potential for the use of

these tools in clinical application. In this study, the clinical translational of the total-body PET/CT scanner resulted in superior imaging outcomes. We utilized a 2-meter total-body PET scanner, which offers a sensitivity approximately 15–68 times greater than that of traditional PET/CT, for our clinical investigation **(32-34).** Moreover, the comprehensive dynamic scanning capability of the scanner facilitated initial investigations into the in vivo distribution and kinetics of **[^{68}Ga]Ga-B7H3-BCH**, enabling the identification of optimal scanning periods. These capabilities have marked benefits for the development of radiopharmaceuticals.

An effective radiotracer must not only exhibit high affinity but also demonstrate stability in vivo, balanced metabolism, and, importantly, optimal tissue uptake, retention, and clearance times to achieve the highest TBR. The modified RESCA-B7H3-BCH, which was improved with PEG4 and Acp, meets these criteria. We have considerable experience in the development of HER2-targeted affinity probes and their clinical translation (35). These modifications improve circulation time, increase water solubility and stability, reduce radiolytic degradation, and minimize the potential damage due to high-temperature labeling processes due to the incorporation of a RESCA moiety. These modifications also reduce renal uptake and expedite excretion. Finally, the modified **[^{68}Ga]Ga-B7H3-BCH** allows the use of a lower radiation dose without compromising affinity.

The **[^{68}Ga]Ga-B7H3-BCH** radiotracer successfully demonstrated specific imaging capabilities across a broad spectrum of malignancies. Positive imaging results were confirmed in a diverse array of cancer types, including lung cancer, melanoma, colon

cancer, lymphoma, liver cancer, stomach cancer, esophageal cancer, rectal cancer, breast cancer, and metastatic lymph nodes of unknown origin. The instances of negative imaging outcomes were consistently associated with low B7H3 expression within lesions. Immunohistochemical analysis of samples from twelve patients revealed varying levels of B7H3 expression, ranging from B7H3 *1+* to B7H3 *3+* expression. The acquisition time of these pathologies and the interval between PET imaging were both within one month, and no drug treatment was administered in between, thus ensuring that there would be no changes in the distribution of the B7H3 target. Given the extensive expression of B7H3 across various malignant tissues, [**^{68}Ga]Ga-B7H3-BCH** has potential for use as a broad-spectrum oncologic imaging agent. Importantly, the excellent performance of the probe in imaging well-differentiated hepatocellular carcinoma and gastric cancer peritoneal metastases highlight promising application possibilities that merit exploration. On the other hand, [**^{68}Ga]Ga-B7H3-BCH** PET imaging can non-invasively validate changes in targets repeatedly, which will play a significant role in the future of B7H3-targeted therapies prior to their implementation.

In foundational experiments, we initially assessed PET images and performed immunohistochemical analyses of five xenograft tumor models, and we observed marked heterogeneity in B7H3 expression within the cells of the individual solid tumors. This variance in B7H3 expression could affect the retention time of imaging probes within tumors, thus influencing the selection of optimal imaging periods and the therapeutic effectiveness of radiopharmaceuticals that are developed using ABYs. Moving forward, we will continue to investigate the impact of these differences on

imaging protocols. In our clinical research, notable effects of differences in B7H3 expression, as determined by tumor immunohistochemistry, were observed in the imaging results. Specifically, differences in B7H3 expression among tumor cells, within the tumor interstitium, and peritumoral tissues led to variable uptake of the probe at tumor sites. Our preliminary conclusions suggest that differences in B7H3 expression among tumor cells markedly influence the uptake of [^{68}Ga]Ga-B7H3-BCH, with differences within the tumor interstitium having the least impact; these findings were inconsistent with our initial expectations. Additionally, B7H3 expression in peritumoral tissues is relatively low and has a minimal impact on imaging. This may suggest that in the use of B7H3-targeted therapies, attention should be focused on the distribution of B7H3 within tumor cells, as high B7H3 expression within the tumor interstitium could mislead clinical evaluations prior to treatment. It would be more appropriate to categorize the expression distribution rather than conflating the two expression patterns. Furthermore, we plan to perform a correlation analysis between the staining of pretreatment tissues with B7H3-targeted ADCs and patient outcomes, aiming to substantiate these findings. Moreover, the utility of this radiotracer will be expanded to predict the effectiveness of B7H3-targeted therapies and evaluate potential resistance to these therapies in the future.

The ABY was taken up in excessive amounts by the kidneys, and the ABY revealed a certain level of B7H3 expression in the liver. Consequently, notably high accumulation of [^{68}Ga]Ga-B7H3-BCH in normal liver and kidney tissues was observed by PET imaging, which interfered with the detection of certain lesions,

526 making PET imaging of renal cancer particularly challenging. Despite a series of

527 chemical modifications to reduce nonspecific uptake in nontarget organs, the ideal

528 biodistribution has not been achieved. On the other hand, dynamic imaging revealed

529 both rapid uptake and clearance of [^{68}Ga]Ga-B7H3-BCH at tumor sites, and delayed

530 imaging did not increase the TBR at these locations. However, the clinical sample size

531 of the multi-tumor imaging analysis in the study was small, which complicates the

532 performance of more in-depth data analysis. Our future plans involve first improving

533 the retention time of the probe at tumor sites, possibly via modifications such as

534 albumin binding or by extending polyethylene glycol chains to increase the molecular

535 weight of the probe, thereby increasing tumor retention. Moreover, we will select tumor

536 types that demonstrate the best imaging results and have the highest clinical diagnostic

537 value for large-scale clinical trials.

538

539

540

541

542

543

544

545

546

547

METHODS

Sex as a biological variable

Among the 20 patients enrolled in this study, 9 were female and 11were male. In this experiment, all experimental mice were female. In this study, sex was not considered as a biological variable

Cell lines and mice

Human H1975 and A549 lung cancer cells were purchased from the Stem Cell Bank, Chinese Academy of Science, and these cells were cultured in DMEM (Biological Industries, Israel). The H1975^{CD276} and A549^{CD276} cell lines were generated via transfection with the full-length CD276 plasmid (Public protein/plasmid library, Nanjing, China) and cultured in DMEM (Sigma Aldrich, USA) supplemented with 1 μg/mL puromycin (Solarbio Life Sciences, Beijing, China). All the media were supplemented with 10% FBS and 1% penicillin–streptomycin from Biological Industries (Israel). The cells were cultured in a humidified incubator at 37 ℃ with 5% CO_2.

Female BALB/c nude mice aged 6–8 weeks were obtained from Vital River (Beijing, China). Approximately 1×10^6 H1975, A549, A549^{CD276}, or H1975^{CD276} cells were suspended in 100 μL of phosphate-buffered saline (PBS, Solarbio, Beijing, China) and subcutaneously injected into the flanks of nude mice to establish a xenograft model. After 2–3 weeks, when the tumor volumes reached approximately 0.5–1 cm^3, the mice were kept under specific pathogen-free conditions and subjected to further experiments. Additionally, six-week-old female Kunming (KM) mice were purchased from Vital

26

River (Beijing, China) and used for the pharmacokinetic, biodistribution and toxicity assays.

Affinity testing assays

A surface plasmon resonance (SPR) experiment was performed to evaluate the binding affinity between the precursor and B7H3 with a Biacore 8K system (Cytiva, Shanghai, China). In brief, after the activation of the nanogold sensor chip with 1-ethyl-3-(3-dimethylaminopropyl) carbodiimide/N-hydroxysuccinimide, the recombinant human B7H3 protein (14058, CST, USA) was immobilized on the chip surface. Next, different concentrations of the precursor were added at a flow rate of 30 μL/min for 240 seconds, and the SPR signal was recorded. The KD, ka and kd values were calculated with Biacore Insight Evaluation 3.0.12.15655 (Biacore Insight Evaluation Software, Beijing, China).

A radioenzyme-linked immunosorbent assay (radio-ELISA) was conducted to determine the binding affinity between the radiopharmaceutical agent and the CD276 protein (Cat: KIT11188, Sino Biological Inc., China). Specifically, 100 μL of the CD276 (1 μg/mL) protein diluted with carbonate coating fluid was added to a 96-well microplate (CLS2481-100EA, Corning, USA) and then incubated at 4 °C overnight. The next day, the microplate was blocked with 5% skim milk and washed with PBST (0.01 mol/L, pH 7.4) (Solarbio, Beijing, China). Then, 50 μL of the radiopharmaceutical agent at different concentrations (0.0037-11.1 MBq/mL, 4 wells/group) was added to the microplate and incubated at 37 °C for 2 hours. The radiopharmaceutical agent was discarded, and after five washes with PBST, the radioactivity of each well was

measured with a γ-counter (PerkinElmer, Wizard2, USA). The one-site total mode in

Graph Pad software (Graph Pad prism 8, USA) was used to fit the relationship between

the molar concentration and radioactivity to calculate the dissociation constant.

Radiolabeling

Both Resca-B7H3-BCH and DOTA-AC12 were synthesized by Tanzhen Bio

(Nanchang, China), ensuring a chemical purity of over 95%. [^{68}Ga]GaCl3 was obtained

from a ^{68}Ge/ ^{68}Ga generator (maximum production 1.85 GBq, ITG, Germany). ^{68}Ga-

labeling was performed by heating 2.5 mL 0.05 M HCl solution (370-740 GBq), 160

μL of 1.0 M sodium acetate (Aladdin, Shanghai, China) and 50 μg Resca-B7H3-BCH

or DOTA-AC12 at 90 °C for 15 minutes. Then, solution was extracted by an activated

C18 column (activation by 10 mL ethanol and 10 mL water) and the radiolabeled ligand

was eluted by 0.5 mL 80% ethanol aqueous solution. After purification, the radiolabeled

ligand was obtained with >99% radiochemical purity analyzed by radio-HPLC. 300-

555 GBq could be obtained with the radiochemical yield of ~75%. The labeling and

quality control of [^{68}**Ga]Ga-B7H3-BCH**] were performed in a GLP environment by

dispensing a hot cell (NMC Ga-68, Tema Sinergie, S.p.A., Italy).

Pharmacokinetics

One hundred microliters (2.96 MBq, 53.3 GBq/μmol) of ^{68}Ga-DOTA-AC12 or

[^{68}**Ga]Ga-B7H3-BCH**] was injected into female KM mice (n=5) via the tail vein. Blood

was collected from the posterior orbital venous plexus at different time points (1, 3, 5,

10, 15, 20, 30, 45, 60, 90, 120, 180, and 240 minutes) and weighed, and radioactivity

was measured with a γ-counter. Additionally, a 1% injection volume was used as the

standard (n=5). The results are expressed as the percentage of the injected dose per gram (%ID/g). The two-phase decay mode in Graph Pad software was used to analyze the blood pharmacokinetics by fitting the %ID/g versus time of the tracers, thus simulating the metabolic process of the radiotracer in vivo.

Biological distribution and radiation dose estimation

For the biological distribution studies, KM mice and A549[CD276] tumor-bearing mice were injected with 37 MBq/kg ^{68}Ga-DOTA-AC12 (200 μL, 53.3 GBq/μmol) or **[⁶⁸Ga]Ga-B7H3-BCH** (200 μL, 53.3 GBq/μmol) via the tail vein (n=3). The mice were sacrificed at different time points. For blocking, one group of A549[CD276] tumor-bearing mice (n=3) was coinjected with 200 μg of unlabeled precursors. Blood and other major organs, including the heart, liver, spleen, lung, kidneys, stomach, small intestine, muscle, bone and brain, were collected and weighed, and radioactivity was measured with a γ-counter. As a standard, 5 samples with an injection dose of 1% were collected, and radioactivity was measured. The results are expressed as the percentage of injected dose per gram (%ID/g).

The fraction of radioactivity uptake by human tissues was calculated according to the biodistribution results in KM mice. The time–activity curves of various organs and the whole body were generated, and the areas under the curves (AUCs) of different organs were calculated with Graph Pad software. OLINDA/EXM software (version 2.2; HERMES Medical Solutions AB) was used to estimate the radiation dosimetry and effective dose for each organ.

PET imaging of tumor-bearing mice

PET/CT imaging of the xenograft tumor model was conducted with small animal PET/CT (Super Nova PET/CT, PINGSENG, Shanghai, China). When the tumor volumes reached 0.5–1 cm^3, the mice were intravenously injected with 200 μL of radiotracer (277.5–370 MBq/kg, 53.3 GBq/μmol) for small-animal PET imaging. Continuous dynamic imaging was performed for 1 hour after administration, and additional imaging was performed at 2 hours or 4 hours. Unlabeled precursor (500 μg) was coinjected into mice bearing A549^{CD276} tumors to establish the blocking control group. After CT-AC PET reconstruction, the images were analyzed with Avatar software, and the SUVmax values of the ROIs, including the kidney, heart, muscle, and tumor, was manually mapped.

Cell uptake and internalization experiments

H1975, A549, A549^{CD276}, or H1975^{CD276} cells were suspended in DMEM and added to 24-well plates (5×10^5 cells/well) one night prior to the uptake experiments or internalization experiments. The uptake experiment was carried out as follows. After the medium was removed, the plates were washed once with PBS (0.01 M). Then, 500 μL of radiopharmaceutical agents diluted with fresh medium (0.074 MBq/well, n=4, 53.3 GBq/μmol) were added to the plates and incubated with the cells at 37 °C for 5 minutes, 30 minutes, 60 minutes or 120 minutes. Then, the plates were washed twice with PBS, and 500 μL of 1 M sodium hydroxide solution was added to lyse the cells. The hydroxide-lysed suspensions were collected, and their radioactivity was measured with a γ-counter. For the blocking control, 50 μg of precursor was coincubated with 500 μL of dilution mixture for 60 minutes, followed by the steps described above. As a

standard, 5 samples with a dilution of 1% were collected, and their radioactivity was

measured.

For the internalization experiment, after 20 minutes of incubation at 37 °C and 4 °C

with a mixture of the tracer (0.074 MBq/500 μL, 53.3 GBq/μmol) and DMEM, the

medium was removed, and the cells were washed two times with cold PBS (0.01 M).

Subsequently, 500 μL of serum-free culture medium was added and incubated with the

cells for 0 hours, 0.5 hours, 1 hour, 2 hours or 4 hours. Then, the dissociated (culture

medium), membrane-bound (0.1 M acetic acid wash), and internalization (1 M NaOH

lysis) fractions were collected. Finally, the radioactivity of each fraction was measured

with a γ-counter, and the internalization rate was calculated.

Western blotting

For Western blotting analysis, a recombinant rabbit monoclonal anti-CD276 primary

antibody (dilution: 1:100, 14058, CST, USA), an anti-GAPDH antibody (1:10000;

A19056, ABCLONAL) and an HRP-conjugated secondary antibody (1:2000; AS014,

ABCLONAL) were used. The final images were processed with an imaging system

(Amersham Imager 680, GE Healthcare, America).

Toxicology experiments

Excessive amounts of the radiopharmaceutical agents (500 μL, 1850 MBq/kg, 53.3

GBq/μmol) were intravenously administered to normal KM mice (n=5). Blood samples

were collected from the periorbital vein at 1 hour, 1 day, 2 days and 7 days postinjection,

and hematological analysis was performed. On the seventh day of the experiment, the

mice were euthanized, and the organs of interest were collected for HE staining. Five

680   mice from the same batch were injected with 500 μL of normal saline and were used as

681   a control group.

Immunohistochemical analysis

683   Immunohistochemical analysis of B7H3 expression was carried out on a Leica BOND

684   III automated immunostainer (Leica Biosystems, Newcastle, UK) with the Bond

685   Polymer Refine Detection Kit (Leica Biosystems, #DS9800). Formalin-fixed paraffin-

686   embedded (FFPE) tissue sections, 4 μm thick, were processed through a series of steps,

687   including deparaffinization, antigen repair, and hydrogen peroxide blocking. The

688   sections were subsequently incubated with the anti-B7H3 primary antibody (dilution:

689   1:100, 14058, CST, USA) for 15 minutes at room temperature. All the slides were

690   independently evaluated by two pathologists. Normal tissue samples (negative for

691   tumors) were obtained from FFPE specimens that were archived in the Department of

692   Peking University Cancer Hospital. The interval between biopsy or surgery and PET

693   scanning for all patients ranged from 2 to 30 days. Four patients had the pathology

694   acquired prior to imaging, and eight patients had the pathology obtained post-imaging.

695   No patients received pharmacological treatment during this period. For each sample,

696   we independently recorded both the staining intensity and the percentage of positive

697   cells within the tumor and intratumoral stroma. The B7H3 staining intensity was

698   categorized as follows: 0 for no staining, 1 for mild membranous staining, 2 for

699   moderate membranous staining, and 3 for strong membranous staining. The

700   histochemistry score (H-score) was calculated by multiplying the percentage of positive

701   cells by the staining intensity, with a maximum score of 300. The samples were further

classified into three categories on the basis of their H-scores: *1+* (H-score < 100), *2+* (H-score 100–200), and *3+* (H-score > 200).

Clinical trial approval and patient eligibility criteria

The important inclusion criteria for oncological patients were as follows: aged between 18 and 75 years and diagnosed with malignant tumors prior to pharmacological treatment and surgery. The important exclusion criteria included the following: severe impairment of liver and kidney function, pregnancy, or lactation. Twenty patients with malignant tumors were enrolled in this study.

Total-body PET/CT imaging

A 194-cm-long axial FOV total-body PET/CT (uEXPLORER, United Imaging Healthcare, Shanghai, China) was used. A low-dose CT scan was performed before the **[^{68}Ga]Ga-B7H3-BCH** injection, and three patients subsequently underwent a total-body dynamic PET scan for 50 minutes after the injection of 1.42 MBq/kg **[^{68}Ga]Ga-B7H3-BCH**. The other 17 patients underwent a static PET/CT scan at 50–60 minutes. Among the subjects, eight patients underwent delayed static scans at 120–125 minutes; among these patients, three underwent dynamic scans, and five had poor lesion visualization or suboptimal imaging outcomes. All the patients underwent an ^{18}F-FDG PET/CT scan at 50–60 minutes with 4.00 MBq/kg. Total-body PET/CT with low-dose CT scans (50 mAs, 140 kVp) were performed for the first scan, and ultralow-dose CT scans (5 mAs, 140 kVp) were performed for delayed scanning.

Total-body PET/CT image reconstruction

723 Three reconstructions were performed: a dynamic reconstruction of data from 0-50

724 minutes, a static reconstruction of data from 45-50 minutes, and a static reconstruction

725 of delayed scans. Dynamic reconstruction included 90 dynamic time frames as follows:

726 0–30 seconds with 2-second frames, 30–180 seconds with 5-second frames, 180–600

727 seconds with 14-second frames, and 600–2280 seconds with 120-second frames. All

728 the time frames were reconstructed with the ordered subset expectation maximization

729 (OSEM) method (4 iterations, 20 subsets), with corrections for the point spread function

730 (PSF) and time of flight (TOF). The dynamic distribution of the ROIs in tumors and

731 major organs was extracted from all 90 frames from 0 to 38 minutes. Static images were

732 reconstructed from list-mode data with vendor-provided software (United Imaging,

733 China), employing an iterative algorithm (20 subsets, 4 iterations) that incorporates

734 TOF information but excludes PSF correction.

735 **[^{68}Ga]Ga-B7H3-BCH biodistribution and dosimetry evaluation in humans**

736 The activity of ^{68}Ga was decay-corrected according to the injection time and normalized

737 to the total activity. Data processing was performed with the vendor-provided software

738 Multi-Modality Workplace (United Imaging, China). To analyze the biodistribution of

739 **[^{68}Ga]Ga-B7H3-BCH**, ROIs were manually delineated on the maximum cross section

740 of major organs/tissues in a 50–60 minute scan. The normal organs/tissues that were

741 selected for volume of interest (VOI) analysis included the salivary glands, kidneys,

742 glands, aorta, esophagus, colon, liver, pancreas, intestines, thyroid, spleen, adrenal

743 glands, eyes, gallbladder, skin, lung and brain. The SUVmax of each ROI was

744 automatically calculated with the vendor's software and was utilized for analysis and

comparison. The SUVmax is defined as:

$$SUVmax = r/(\frac{a'}{w})$$

where r is the maximum radioactivity activity concentration (kBq/mL) as measured by the PET scanner within the defined ROI, a' is the decay-corrected amount (kBq), and w is the weight of the patient (g).

ROC curves

Tumor tissues were collected from 12 patients and included in the ROC curve analysis. The tumor tissues were initially subjected to immunohistochemical staining for the B7H3 protein. According to the expression results, the samples were categorized as B7H3 *1+*, B7H3 *2+*, or B7H3 *3+*, resulting in 32 positive lesions (from 8 patients) and 8 negative lesions (from 4 patients). For each lesion, the SUVmax at 50–60 minutes for **[⁶⁸Ga]Ga-B7H3-BCH** PET and the SUVmax for ¹⁸F-FDG PET were analyzed. Owing to the inability to obtain pathological biopsies from all lesions, we assumed in our statistical analysis that the primary and metastatic lesions in the enrolled patients shared equivalent B7-H3 expression levels on the basis of their homogeneity, and these SUVmax values were paired with the B7H3 scores of each lesion to generate ROC curves.

Statistical analysis

Statistical analysis was performed with Prism (V8.0, GraphPad Software, New Zealand) and Origin software (V2018, Microcal, USA). The statistical results have validated and met the pre-specified primary endpoint of registered trial. The fluorescence intensity,

cellular uptake, blood biochemical parameters, tumor xenograft biodistribution, and other comparative data of two independent samples were analyzed by unpaired Student's t tests. $P < 0.05$ was considered to indicate a significant difference. Organ uptake data in the form of the SUVmax were grouped by sex and age. To compare distributions between samples, continuous variables are presented as the means $\pm$ standard deviations. The SUVmax and TLR of **[^{68}Ga]Ga-B7H3-BCH** and ^{18}F-FDG PET/CT were compared using the paired-samples t test (normally distributed variables). A hypothesis test on a linear mixed effect model to assert the differences in the SUVmean and SUVmax values among the three groups corresponding to the pathological grades of all lesions. $P < 0.005$ was considered to indicate a significant difference. The criteria for determining the optimal cutoff value of **[^{68}Ga]Ga-B7H3-BCH** were the point on the ROC curve that was closest to the upper left corner of the unit square and the point that had the highest Youden index (sensitivity + specificity). The total AUC and its 95% CI were calculated. The sensitivity and specificity were calculated as indicators for predicting B7H3 expression.

Study approval

All the animal experiments were approved by the Ethics Committee of Peking University Cancer Hospital (approval number: EAEC 2023–18). The clinical study was approved by the Ethics Committee of Peking University Cancer Hospital (approval number: 2023KT131), and this study was registered on ClinicalTrials.gov (NCT06454955). Written informed consents were obtained from all participants.

Data availability statement

788   All relevant data are within the manuscript and its supplementary information files,

789   including the supporting data values XLS file.

790

791

792

793

794

795

796

797

798

799

800

801

802

803

804

805

806

807

808

809

AUTHOR CONTRIBUTIONS

X.L. was responsible for the overall design of the experiment, participated in and completed the experiments, wrote the main manuscript text, and provided funding support. W.Y., Z.L.X. and J.L. performed the immunohistochemical staining and analysis of the mouse and human tissue sections. R.Y.N. participated in and completed the basic experiments. W.Z. collected and analyzed the patients' clinical information. Z.N.N., M.X.X. and Z.H. provided technical support for the PET/CT imaging equipment, image processing, and clinical diagnosis. Z.W.Y. and H.C.X. provided the CD276-transfected cells and conducted the Western blotting analysis. Y.Z. participated in the experimental design and the writing and revision of the manuscript. All the authors reviewed the manuscript.

Regarding the order of the first authors: X.L. initiated the research, completed most of the experiments, and wrote the majority of the manuscript and thus is listed first; W.Y. performed extensive staining and analysis of immunohistochemical sections from patients, which constituted a portion of the content of the article and thus is listed second; R.Y.N. primarily conducted the foundational experiments for basic research, playing a key role in the early stages of the study, and thus is listed third; finally, W.Z. was responsible for communicating with clinical patients, screening and enrolling participants, and performing some data analysis, and thus is listed fourth.

REFERENCES

1. Kontos F, et al. B7-H3: An Attractive Target for Antibody-based Immunotherapy. *Clin Cancer Res*, 2021; 27(5): 1227-1235.

2. Getu A A, et al. New frontiers in immune checkpoint B7-H3 (CD276) research and drug development. *Mol Cancer*, 2023; 22(1): 43.

3. Seaman S, et al. Eradication of Tumors through Simultaneous Ablation of CD276/B7-H3-Positive Tumor Cells and Tumor Vasculature. *Cancer Cell*, 2017; 31(4): 501-515.

4. Dong P, et al. B7H3 As a Promoter of Metastasis and Promising Therapeutic Target. *Front Oncol*, 2018; 8: 264.

5. Majzner R G, et al. CAR T Cells Targeting B7-H3, a Pan-Cancer Antigen, Demonstrate Potent Preclinical Activity Against Pediatric Solid Tumors and Brain Tumors. *Clin Cancer Res*, 2019; 25(8): 2560-2574.

6. Huang Y, et al. FUT8-mediated aberrant N-glycosylation of B7H3 suppresses the immune response in triple-negative breast cancer. *Nat Commun*, 2021; 12(1): 2672.

7. Kraan J, et al. Endothelial CD276 (B7-H3) expression is increased in human malignancies and distinguishes between normal and tumour-derived circulating endothelial cells. *Br J Cancer*, 2014; 111(1): 149-56.

8. Seaman S, et al. Genes that distinguish physiological and pathological angiogenesis. *Cancer Cell*, 2007; 11(6): 539-54.

9. Agarwal S, et al. Tumor-derived biomarkers predict efficacy of B7H3 antibody-drug conjugate treatment in metastatic prostate cancer models. *J Clin Invest*, 2023; 133(22):

e162148.

10. Kendsersky N M, et al. The B7-H3-Targeting Antibody-Drug Conjugate m276-SL-PBD Is Potently Effective Against Pediatric Cancer Preclinical Solid Tumor Models. *Clin Cancer Res*, 2021; 27(10): 2938-2946.

11. Passaro A, et al. Antibody-Drug Conjugates in Lung Cancer: Recent Advances and Implementing Strategies. *J Clin Oncol*, 2023; 41(21): 3747-3761.

12. Chu C E, et al. Heterogeneity in NECTIN4 Expression Across Molecular Subtypes of Urothelial Cancer Mediates Sensitivity to Enfortumab Vedotin. *Clin Cancer Res*, 2021; 27(18): 5123-5130.

13. Wolf Y, et al. UVB-Induced Tumor Heterogeneity Diminishes Immune Response in Melanoma. *Cell*, 2019; 179(1): 219-235.e21.

14. Bensch F, et al. [89]Zr-atezolizumab imaging as a non-invasive approach to assess clinical response to PD-L1 blockade in cancer. *Nat Med*, 2018; 24(12): 1852-1858.

15. Duan X, et al. First-in-Human Study of the Radioligand ^{68}Ga-N188 Targeting Nectin-4 for PET/CT Imaging of Advanced Urothelial Carcinoma. *Clin Cancer Res*, 2023; 29(17): 3395-3407.

16. Lee I K, et al. Monitoring Therapeutic Response to Anti-FAP CAR T Cells Using [^{18}F]AlF-FAPI-74. *Clin Cancer Res*, 2022; 28(24): 5330-5342.

17. Kramer K, et al. Phase 1 study of intraventricular ^{131}I-omburtamab targeting B7H3 (CD276)-expressing CNS malignancies. *J Hematol Oncol*, 2022; 15(1): 165.

18. Burvenich I J G, et al. Molecular imaging of T cell co-regulator factor B7-H3 with [89]Zr-DS-5573a. *Theranostics*, 2018; 8(15): 4199-4209.

898   19. Descotes J. Immunotoxicity of monoclonal antibodies. *MAbs*, 2009; 1(2): 104-111.

899   20. Loktev A, et al. A Tumor-Imaging Method Targeting Cancer-Associated Fibroblasts.

900   *J Nucl Med*, 2018; 59(9): 1423-1429.

901   21. Ruigrok E a M, et al. Extensive preclinical evaluation of lutetium-177-labeled

902   PSMA-specific tracers for prostate cancer radionuclide therapy. *Eur J Nucl Med Mol*

903   *Imaging*, 2021; 48(5): 1339-1350.

904   22. Löfblom J, et al. Affibody molecules: engineered proteins for therapeutic,

905   diagnostic and biotechnological applications. *FEBS Lett*, 2010; 584(12): 2670-2680.

906   23. Tolmachev V, Orlova A. Affibody Molecules as Targeting Vectors for PET Imaging.

907   *Cancers (Basel)*, 2020; 12(3): 651.

908   24. Frejd F Y, Kim K T. Affibody molecules as engineered protein drugs. *Exp Mol Med*,

909   2017; 49(3): e306.

910   25. Stern L A, et al. Cellular-Based Selections Aid Yeast-Display Discovery of Genuine

911   Cell-Binding Ligands: Targeting Oncology Vascular Biomarker CD276. *ACS Comb Sci*,

912   2019; 21(3): 207-222.

913   26. Oroujeni M, et al. Evaluation of affinity matured Affibody molecules for imaging

914   of the immune checkpoint protein B7-H3. *Nucl Med Biol*, 2023; 124-125: 108384.

915   27. Bam R, et al. Efficacy of Affibody-Based Ultrasound Molecular Imaging of

916   Vascular B7-H3 for Breast Cancer Detection. *Clin Cancer Res*, 2020; 26(9): 2140-2150.

917   28. Oroujeni M, et al. Evaluation of an Affibody-Based Binder for Imaging of Immune

918   Check-Point Molecule B7-H3. *Pharmaceutics*, 2022; 14(9): 1780.

919   29. Code of Federal Regulations Title 21, Part 361: Radioactive Drugs for Certain

920   Research Uses. *Food and drug administration (FDA)*, 2024; 5.

921   30. Macgregor H L, et al. High expression of B7-H3 on stromal cells defines tumor and

922   stromal compartments in epithelial ovarian cancer and is associated with limited

923   immune activation. *J Immunother Cancer*, 2019; 7(1): 357.

924   31. Liu H J, et al. mTORC1 upregulates B7-H3/CD276 to inhibit antitumor T cells and

925   drive tumor immune evasion. *Nat Commun*, 2023; 14(1): 1214.

926   32. Badawi R D, et al. First Human Imaging Studies with the EXPLORER Total-Body

927   PET Scanner. *J Nucl Med*, 2019; 60(3): 299-303.

928   33. Cherry S R, et al. Total-body imaging: Transforming the role of positron emission

929   tomography. *Sci Transl Med*, 2017; 9(381): eaaf6169.

930   34. Zhang X, et al. Subsecond total-body imaging using ultrasensitive positron emission

931   tomography. *Proc Natl Acad Sci U S A*, 2020; 117(5): 2265-2267.

932   35. Guo X, et al. Comparison of an Affibody-based Molecular Probe and ^{18}F-FDG for

933   Detecting HER2-Positive Breast Cancer at PET/CT. *Radiology*, 2024; 311(3): e232209.
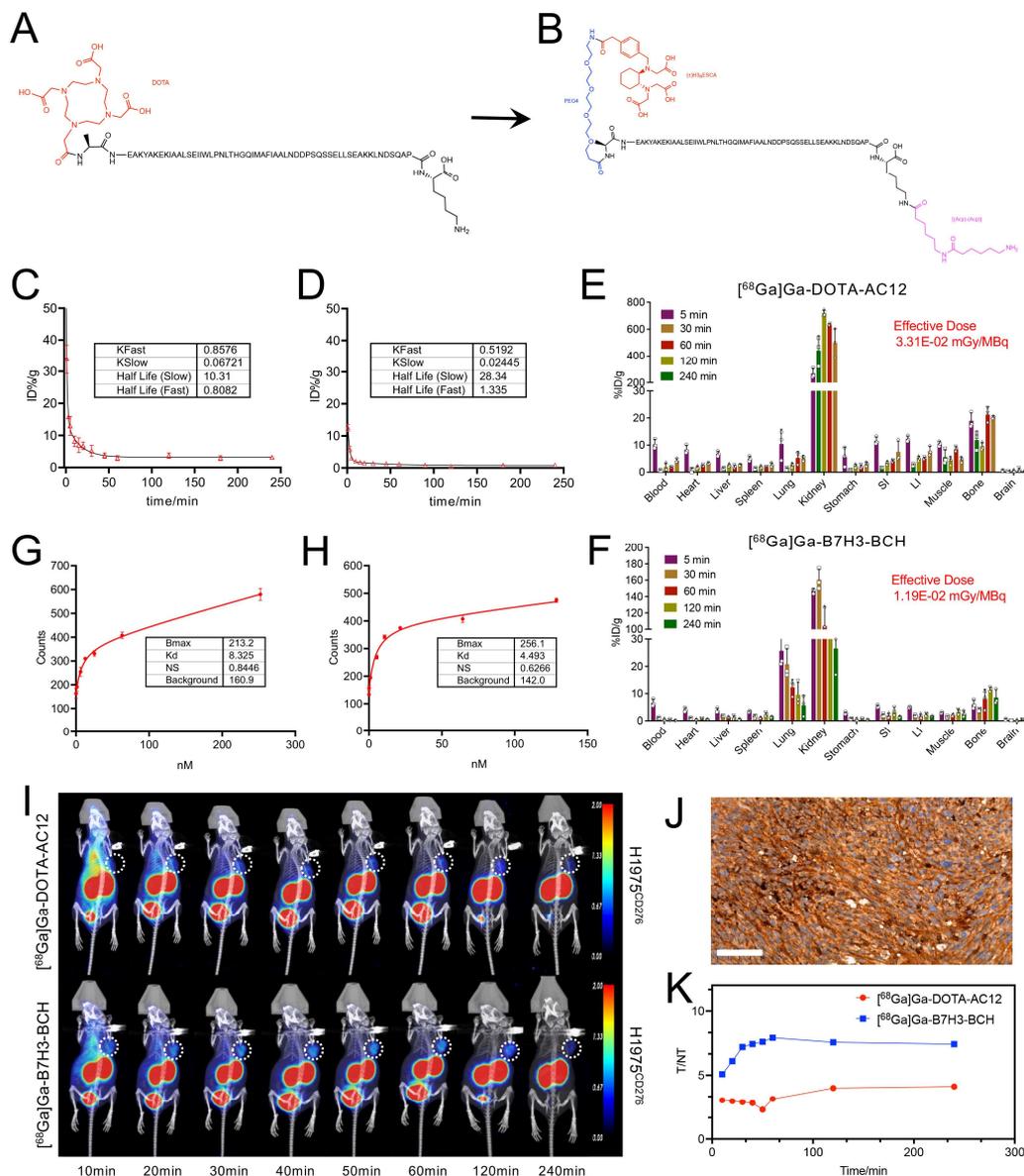
934

935

936

937

938

939

940

941

943

Fig. 1 Affibody improvement, synthesis and quality control. **A** Chemical structure of DOTA-AC12. **B** Chemical structure of the improved Resca-B7H3-BCH. **C** Pharmacokinetic parameters of ^{68}Ga-DOTA-AC12 in vivo. **D** Pharmacokinetic parameters of **[^{68}Ga]Ga-B7H3-BCH** in vivo. **E F** Distribution and radiation dose estimation of ^{68}Ga-DOTA-AC12 and **[^{68}Ga]Ga-B7H3-BCH** in mice. **G** The binding affinity assays of ^{68}Ga-DOTA-AC12. **H** The binding affinity assays of **[^{68}Ga]Ga-B7H3-BCH**. **I** Head-to-head dynamic PET/CT imaging using ^{68}Ga-DOTA-AC12 and **[^{68}Ga]Ga-B7H3-BCH** in an H1975^{CD276} xenograft model. **J** B7H3 immunohistochemistry of H1975^{CD276} tumor slice (Scale bar=100μm). **K** Dynamic changes in tumor to muscle ratio (T/NT) by analyzing the SUVmax of ^{68}Ga-DOTA-AC12 and **[^{68}Ga]Ga-B7H3-BCH** PET/CT images.

953
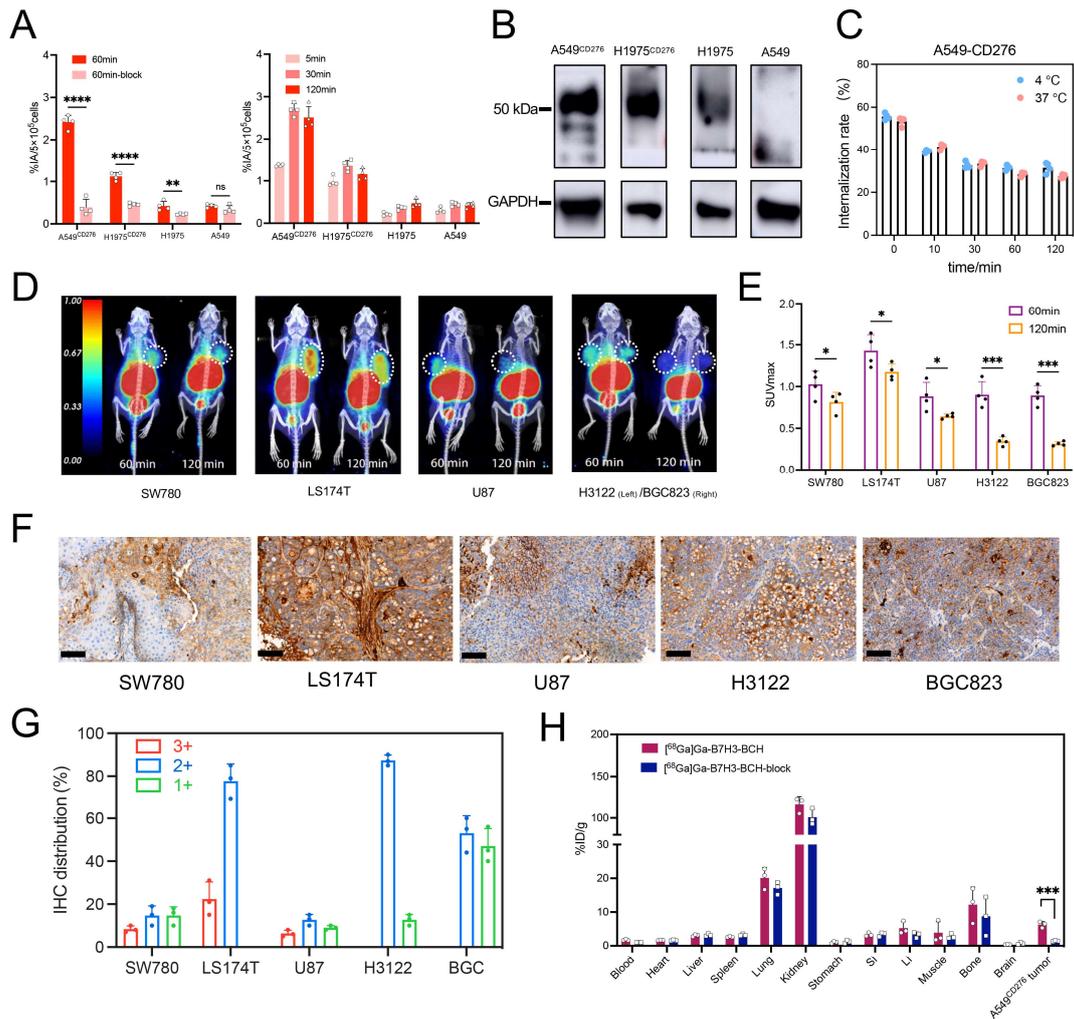
Fig. 2 Functional testing of [⁶⁸Ga]Ga-B7H3-BCH radiotracer. **A** Cellular uptake and inhibition uptake of [⁶⁸Ga]Ga-B7H3-BCH in B7H3-transfected and un-transfected human lung cancer cells at different time points. Data are presented as mean ± standard deviation (n = 4). $^{ns}P > 0.05$, $**P < 0.01$, $****P < 0.0001$. **B** Expression of B7H3 protein in four cell lines by Western blot analysis. Glyceraldehyde-3-phosphate dehydrogenase (GAPDH) was used as the loading control. **C** Cellular internalization of [⁶⁸Ga]Ga-B7H3-BCH in A549^CD276 cells. **D** PET/CT imaging of five different xenograft models—SW780, LS174T, U87, H3122, and BGC823 tumors at 1 and 2 hour post-injection. **E** Statistical analysis of SUVmax over time for the tumor region of interest (ROI) across various time points. Data are presented as mean ± standard deviation (n = 4). $*P < 0.05$, $***P < 0.001$. **F** Immunohistochemistry (IHC) staining of the five tumor slices (Scale bar=100μm). **G** Grading of IHC regions in five tumor sections, classified by staining intensity into B7H3 *3+*, B7H3 *2+*, and B7H3 *1+*. Statistical analysis was conducted based on the proportion of B7H3 expression intensity across different regions. **H** Biodistribution and inhibited biodistribution of [⁶⁸Ga]Ga-B7H3-BCH in an A549^CD276 tumor model. Data are presented as mean ± standard deviation (n = 3). $***P < 0.001$.
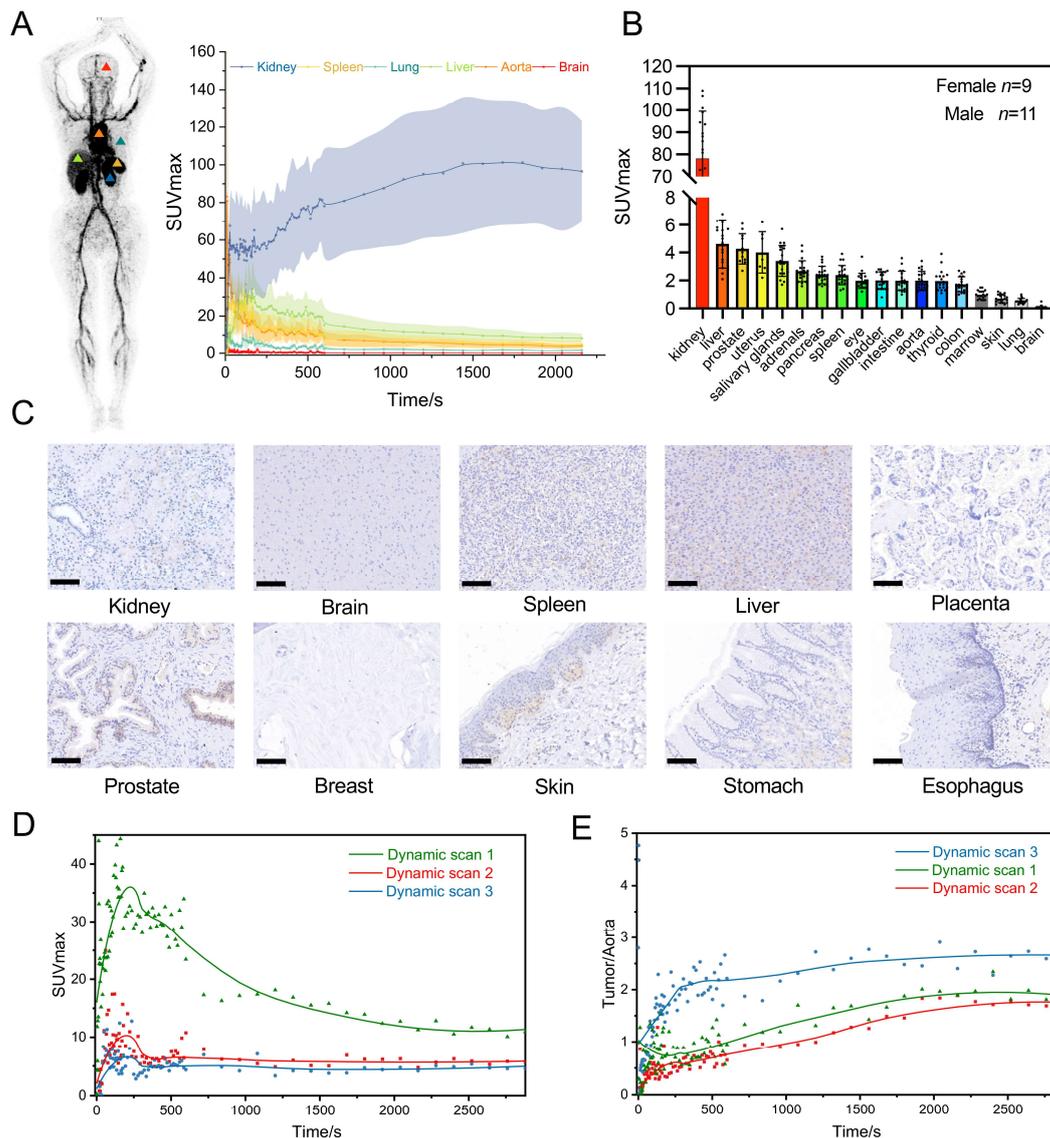
969

970
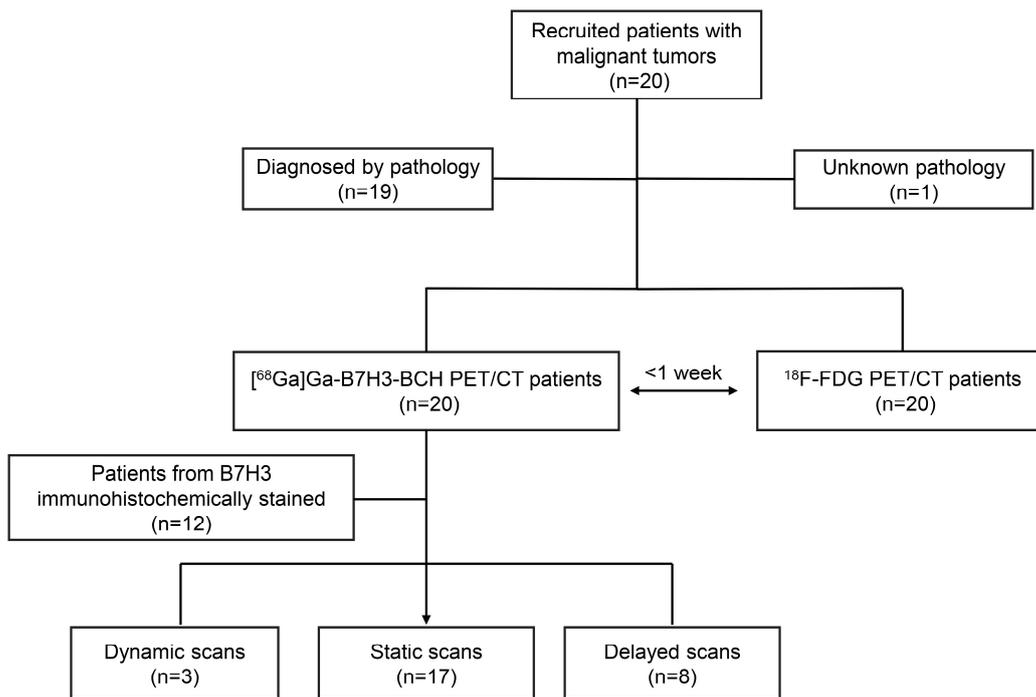
971

972 **Fig. 3** The flow diagram of clinical study design and scanning methods.

973

974

975
976 **Fig. 4** Dynamic PET imaging analysis. **A** The 30s dynamic PET imaging of patient, and the dynamic
977 changes of selected organs at 0 to 35 min with SUVmax (n = 3). **B** Rank ordering of **[⁶⁸Ga]Ga-**
978 **B7H3-BCH** uptake in different organs at 50-60 min static PET imaging indicated by SUVmax (n
979 =20). **C** IHC staining of B7H3 expression in normal human organ tissue slices. (Scare bar=100 μM)
980 **D** The dynamic changes of tumor lesions at 0-50 min dynamic PET imaging from three
981 representative patients. **E** The dynamic changes of tumor-to-aorta radio with the metastatic lesions
982 at 0-50 min dynamic PET imaging from three representative patients.

983
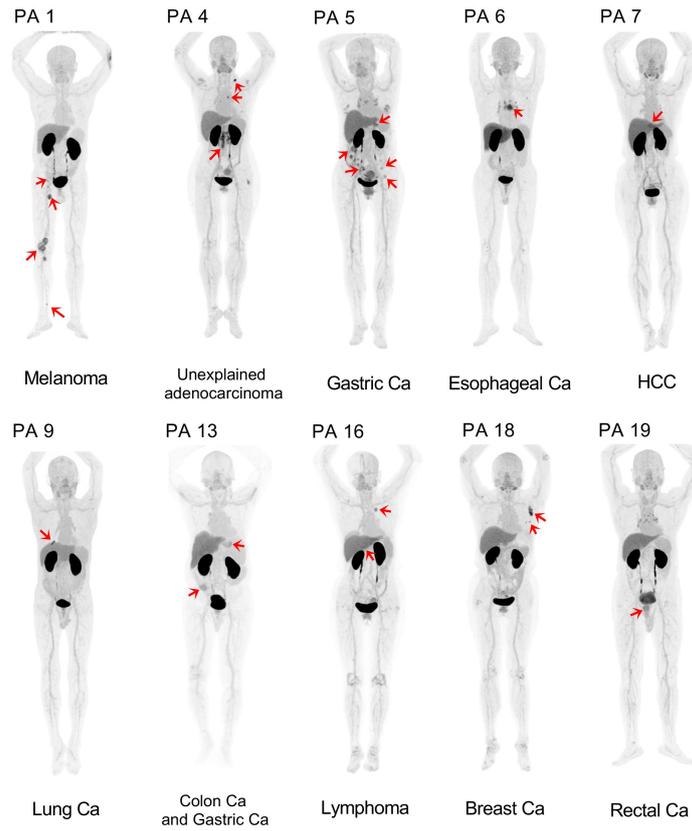
Fig.5 Maximum intensity projection (MIP) images from **[⁶⁸Ga]Ga-B7H3-BCH** PET scans of ten different tumor patients, with red arrows highlighting both primary and metastatic lesions.
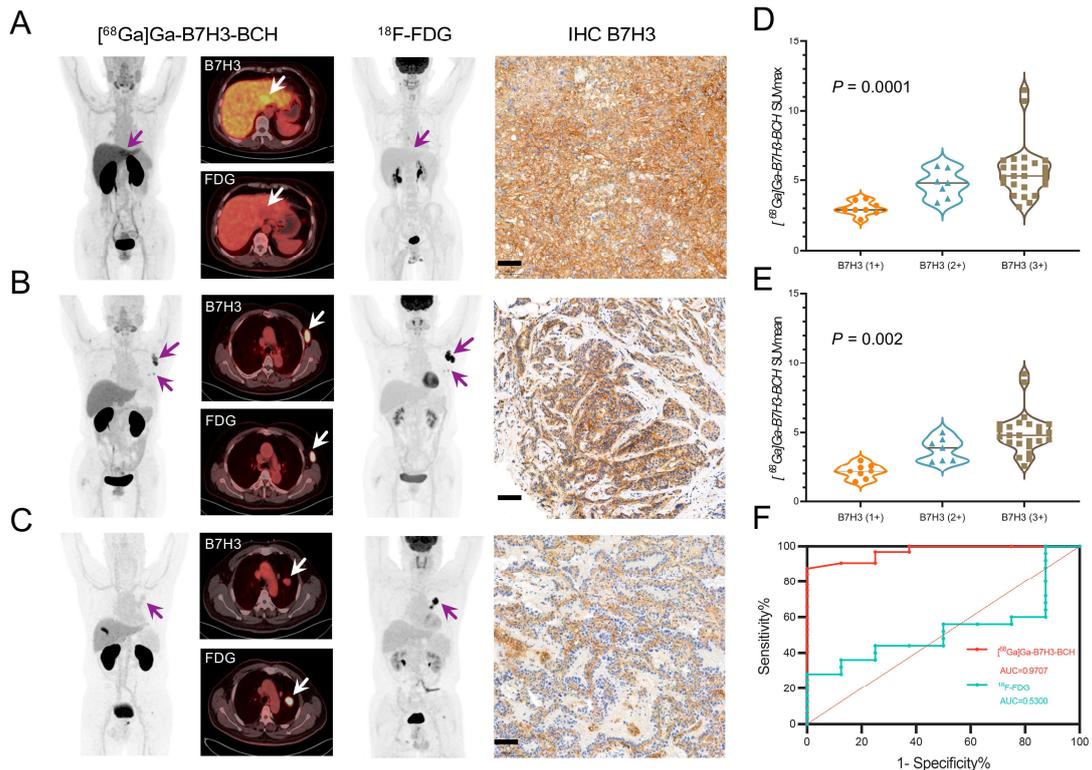
Fig.6 Correlation between PET/CT imaging and B7H3 protein expression. **A** Head-to-head **[⁶⁸Ga]Ga-B7H3-BCH** and ¹⁸F-FDG PET/CT images and IHC staining of a liver cancer patient (this case corresponds to PA 7 in Fig. 4) with high B7H3 expression across three different B7H3 expression levels. IHC score is B7H3 *3+*, Scale bar=100μm. **B** Head-to-head PET imaging of a breast cancer patient (this case corresponds to PA 18 in Fig. 4) with moderate to high B7H3 expression. IHC score is B7H3 *2+*, Scale bar=100μm. **C** Head-to-head PET imaging of a lung cancer patient with low B7H3 expression. IHC score is B7H3 *1+*, Scale bar=100μm. **D E** Box plots depicting the SUVmax and SUVmean of **[⁶⁸Ga]Ga-B7H3-BCH** for all 40 lesions in 12 patients with B7H3 *3+*, B7H3 *2+*, and B7H3 *1+* by IHC staining. Statistical significance was indicated using a hypothesis test on a linear mixed effect model ($P < 0.005$ was considered significant). **F** Receiver operating characteristic curve illustrating the sensitivity and specificity of **[⁶⁸Ga]Ga-B7H3-BCH** and ¹⁸F-FDG in evaluating B7H3 expression.
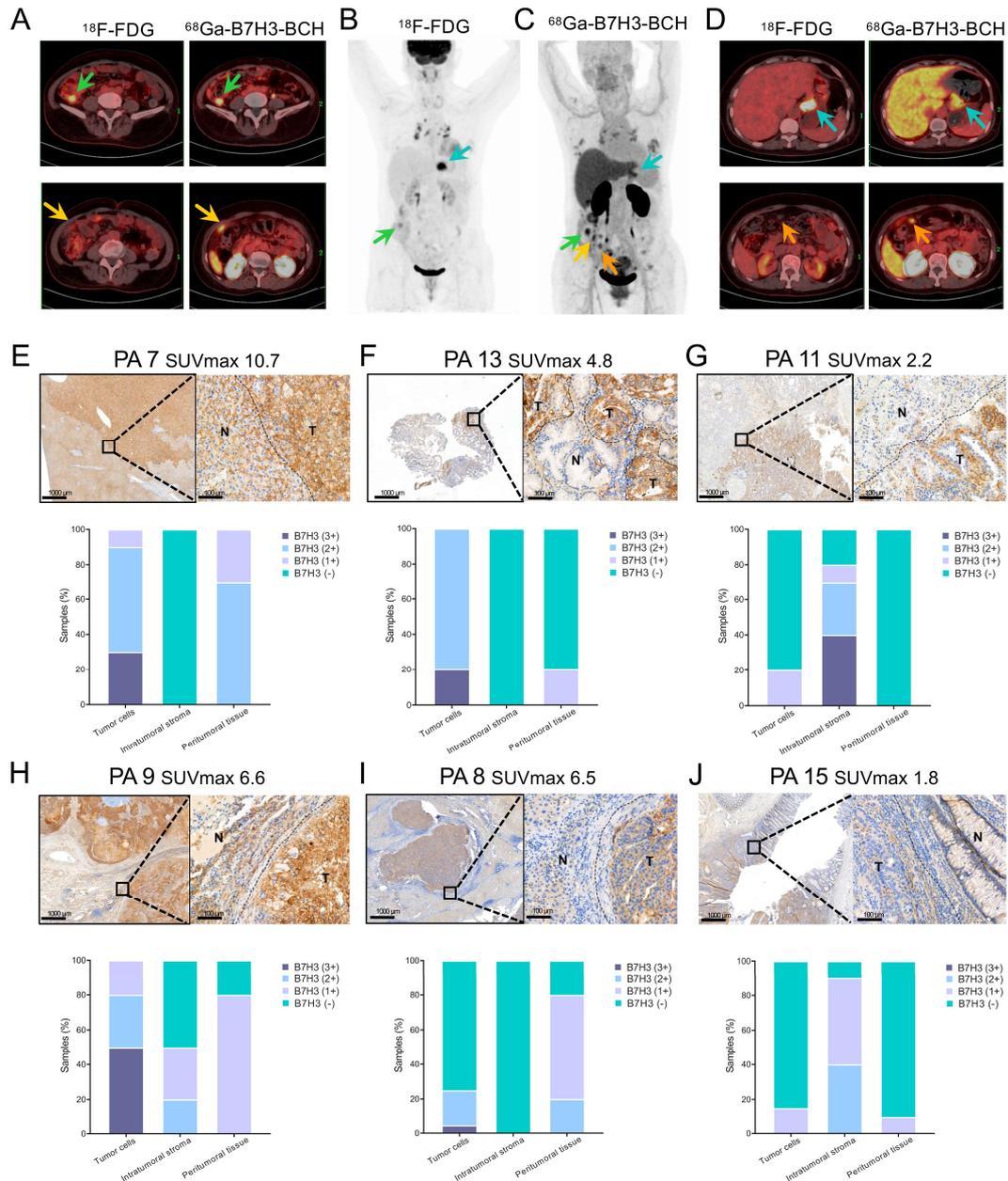
Fig. 7 Advantages imaging and influence of variable B7H3 expression. **A-D** Maximum intensity projection and selected axial PET/CT images of a gastric cancer patient (this case corresponds to PA 5 in Fig. 4) with multiple peritoneal metastases, comparing ^{18}F-FDG and **[^{68}Ga]Ga-B7H3-BCH** imaging. **E** Immunohistochemical analysis at the tumor margin in a liver cancer biopsy, including tumor cells, intratumoral stroma, and peritumoral tissue with B7H3 expression graded as *3+*, *2+*, *1+*, and negative. 'T' represents the tumor region, 'N' denotes the non-tumor cell area, and dashed lines indicate the boundaries. **F-J** Immunohistochemical imaging and data analysis at the tumor margin in a gastric cancer biopsy, two lung cancer biopsies, a liver cancer biopsy, and a colon cancer biopsy, respectively.

TABLES

1015 **Table. 1** Information on Enrolled Study Participants

Characteristic	Total	Percentage (%)
Participants	20	100
Sex		
Female	9	45
Male	11	55
Age(y)		
Mean±SD	62±9	
Range	36-75	
Scan Methods		
^{18}F-FDG+**[^{68}Ga]Ga-B7H3-BCH**	20	100
Dynamic scan	3	15
Static scan	17	85
Delay scan	8	40
Pathological and immunohistochemistry		
Total slices	12	60
B7H3 *3+*	5	42
B7H3 *2+*	3	25
B7H3 *1+*	4	33
Tumor type		
Lung cancer	4	20
melanoma	3	15
colon cancer	2	10
lymphoma	2	10
liver cancer	2	10
esophageal cancer	2	10
stomach cancer	1	5
metastatic lymph nodes of unknown origin	1	5
rectal cancer	1	5
breast cancer	1	5
stomach cancer and colon cancer	1	5

1016

1017

1018

1019 **Table. 2** Comparison of [^{68}Ga]Ga-B7H3-BCH and ^{18}F-FDG PET/CT Based on Tracer

1020 Uptake and TMR of Lesions

Tumor types	SUVmax			TMR		
	^{68}Ga-B7H3	^{18}F-FDG	*P*	^{68}Ga-B7H3	^{18}F-FDG	*P*
Lung CA	4.2 (2.2-7.0)	8.2 (5.4-16.7)	0.13	10.9 (4.4-17.5)	14.4 (6.8-33.4)	0.54
Melanoma	4.9 (4.4-5.2)	16.8 (3-38.4)	<0.001	16.3 (14.7-17.3)	21.2 (3.8-41.3)	0.17
Colorectal CA	4.5 (4-5.4)	7.5 (2.5-15.7)	0.52	11.5 (10.3-13.3)	8.4 (3.6-15.7)	0.47
Lymphoma	4.5 (3.3-6)	17.4 (8.3-24.1)	0.003	11.4 (8.3-15.0)	21.8 (10.4-30.1)	0.03
Liver CA	7.0 (3.9-10.7)	3.6 (2.2-4.6)	0.18	12.9 (6.5-21.4)	5.8 (3.1-7.7)	0.20
Esophageal CA	4.4 (3.6-6.4)	10.2 (2.9-16.6)	0.09	10.1 (7.2-16.0)	13.1 (3.2-18.4)	0.48
Stomach CA	5.3 (3.7-6.2)	5.9 (1.1-17.0)	0.75	9.2 (7.4-10.7)	8.4 (1.6-24.3)	0.74
Breast CA	4.9 (3.4-6.0)	17.5 (5.3-33.3)	0.08	12.3 (8.5-14.8)	29.2 (8.7-55.5)	0.14

Data are median and range. Paired-samples t test was performed.

1021

1022

1023

1024